

Pressure-induced formation of rhodium zigzag chains in the honeycomb rhodate Li_2RhO_3

V. Hermann, S. Biswas, Jihaan Ebad-Allah, F. Freund, Anton Jesche, Alexander A. Tsirlin, M. Hanfland, D. Khomskii, Philipp Gegenwart, R. Valentí, Christine A. Kuntscher

Angaben zur Veröffentlichung / Publication details:

Hermann, V., S. Biswas, Jihaan Ebad-Allah, F. Freund, Anton Jesche, Alexander A. Tsirlin, M. Hanfland, et al. 2019. "Pressure-induced formation of rhodium zigzag chains in the honeycomb rhodate Li_2RhO_3 ." *Physical Review B* 100 (6): 064105. <https://doi.org/10.1103/physrevb.100.064105>.

Pressure-induced formation of rhodium zigzag chains in the honeycomb rhodate Li_2RhO_3

V. Hermann,¹ S. Biswas,² J. Ebad-Allah,^{1,3} F. Freund,⁴ A. Jesche,⁴ A. A. Tsirlin,⁴ M. Hanfland,⁵ D. Khomskii,⁶ P. Gegenwart,⁴ R. Valentí,² and C. A. Kuntscher^{1,*}

¹Experimentalphysik II, Augsburg University, 86159 Augsburg, Germany

²Institut für Theoretische Physik, Goethe-Universität Frankfurt, 60438 Frankfurt am Main, Germany

³Department of Physics, Tanta University, 31527 Tanta, Egypt

⁴Experimentalphysik VI, Center for Electronic Correlations and Magnetism, Augsburg University, 86159 Augsburg, Germany

⁵European Synchrotron Radiation Facility, Boîte Postale 220, 38043 Grenoble, France

⁶II. Physikalisches Institut, Universität zu Köln, Zùlpicher Strasse, 77, 50937 Köln, Germany



(Received 7 May 2019; published 28 August 2019)

We use powder x-ray diffraction to study the effect of pressure on the crystal structure of the honeycomb rhodate Li_2RhO_3 . We observe low-pressure ($P < P_{c1} = 6.5$ GPa) and high-pressure ($P > P_{c2} = 14$ GPa) regions corresponding to the monoclinic $C2/m$ symmetry, while a phase mixture is observed at intermediate pressures. At $P > P_{c2}$, the honeycomb structure becomes distorted and features short Rh-Rh bonds forming zigzag chains stretched along the crystallographic a direction. This is in contrast to dimerized patterns observed in triclinic high-pressure polymorphs of $\alpha\text{-Li}_2\text{IrO}_3$ and $\alpha\text{-RuCl}_3$. Density-functional theory calculations at various pressure conditions reveal that the observed rhodium zigzag-chain pattern is not expected under hydrostatic pressure but can be reproduced by assuming anisotropic pressure conditions.

DOI: [10.1103/PhysRevB.100.064105](https://doi.org/10.1103/PhysRevB.100.064105)

I. INTRODUCTION

In recent years, $4d$ and $5d$ transition-metal compounds were intensively studied due to their extremely rich physics. In comparison to $3d$ compounds, where the electronic correlation U dominates over the spin-orbit coupling constant λ_{SOC} and Hund's coupling J_{H} , spin-orbit coupling (SOC) becomes more and more important for $4d$ and $5d$ transition-metal compounds, whereas the strength of electronic correlations decreases. The actual physics of these compounds thereby depends on a delicate balance between U , λ_{SOC} , and J_{H} , as well as the crystal structure. The class of layered honeycomb-type $4d$ and $5d$ transition-metal compounds, such as $A_2\text{MO}_3$ ($A = \text{Li}, \text{Na}$ and $M = \text{Ir}, \text{Rh}$) and $\alpha\text{-RuCl}_3$, is especially interesting in this regard, as this delicate balance of parameters was discussed in terms of Kitaev physics and a possible spin-liquid state [1–9]. However, in Na_2IrO_3 , $\alpha\text{-Li}_2\text{IrO}_3$, and $\alpha\text{-RuCl}_3$ the quantum spin-liquid ground state is not realized since these materials were found to order magnetically at low temperatures [4,10–12].

As for Li_2RhO_3 , its magnetic ground state is still under debate. No long-range magnetic order could be found down to ≈ 0.5 K, but instead, at small magnetic fields spin freezing was observed below 6–7 K [8,9], although it is suspected that the majority of magnetic moments form a fluctuating liquidlike state [9]. Whether this partial spin freezing is due to proximity to the Kitaev quantum spin-liquid ground state or due to unavoidable defects (antisite disorder and/or stacking faults) is still unclear [9,13]. However, *ab initio* and effective-model calculations showed that Li_2RhO_3 bears electronic structure

similar to the iridates [14] and hosts anisotropic Kitaev interaction terms of the same magnitude as in $5d$ iridates [13]. According to electrical resistivity measurements, Li_2RhO_3 is insulating at ambient pressure [8,14].

Another interesting aspect of Li_2RhO_3 is its behavior under pressure, where honeycomb iridates [15,16] and $\alpha\text{-RuCl}_3$ [17,18] become dimerized and, consequently, nonmagnetic. Previously [15], we showed that the size of the central ion, the strength of the spin-orbit coupling, electronic correlations, and Hund's coupling all act against the dimerization. In comparison to $\alpha\text{-Li}_2\text{IrO}_3$, λ_{SOC} in Li_2RhO_3 is expected to be lower, while the electronic correlations should be enhanced in Rh^{4+} compared to Ir^{4+} , as screening by oxygen orbitals is reduced. Therefore, one generally expects a higher transition pressure in Li_2RhO_3 and a larger pressure range for tuning the putative Kitaev magnetism of this compound. Here, we show that this is the case and also that the pressure-induced transformations are very different from the dimerization observed in honeycomb iridates.

II. METHODS

A. Experimental details

A powder sample of Li_2RhO_3 was prepared by a solid-state reaction of Li_2CO_3 and Rh in oxygen flow at 850°C with several intermediate regrindings. The sample quality was confirmed by laboratory x-ray diffraction using the Rigaku MiniFlex diffractometer (Cu $K\alpha$ radiation, Bragg-Brentano geometry). This synthesis procedure yield samples with the best structural order achieved so far [19], although stacking faults are still present. Their concentration is discussed in Sec. III A.

*christine.kuntscher@physik.uni-augsburg.de

Li_2RhO_3 powder was loaded into a diamond anvil cell (DAC) for pressure generation, and helium was used as a pressure-transmitting medium. The powder x-ray diffraction patterns were obtained using synchrotron radiation at beamline ID15B at the European Synchrotron Radiation Facility (ESRF), Grenoble, at room temperature. The wavelength of the radiation was 0.411267 \AA , and the patterns were obtained in the 2θ range between 2° and 33° . The pressure in the DAC was determined *in situ* by the ruby luminescence method. The resulting patterns were analyzed by Rietveld refinements using the JANA2006 software [20]. The quality of the fit is gauged by the profile factor R_p , as defined in Ref. [21], and by the commonly used weighted profile factor $R_{wp} = \{\sum_i w_i [y'_i(\text{obs}) - y'_i(\text{calc})]^2\} / \{\sum_i w_i y'_i(\text{obs})^2\}$, where y'_i are intensities corrected for background. The absorption correction for a cylindrical sample was calculated to be lower than the value 1 (using Ref. [22]), so no absorption correction was applied. The isotropic atomic displacement parameters U_{iso} were fixed to the value of 0.005 \AA^2 for all atomic positions, except for Rh(1) and Li(1).

B. Computational details

Structural optimizations were performed under different pressure conditions by using the projector augmented plane wave [23] method based on density-functional theory (DFT), as implemented in the VASP package [24]. Calculations were done within the generalized gradient approximation (GGA), GGA+ U [25], and GGA+SOC+ U (including spin-orbit coupling effects for Rh). The value of the on-site Coulomb parameter U was chosen based on the reproducibility of the experimental structure, as will be shown below. The cutoff for the wave function was set at 650 eV. K -point meshes of size $8 \times 6 \times 8$ were used for all the structural optimizations.

We performed two types of structural optimizations: (i) allowing relaxation of both lattice parameters and atomic positions under fixed hydrostatic pressure, which we refer to as “full relaxation,” and (ii) keeping the lattice parameters fixed according to given pressure conditions and allowing the relaxation of only the atomic positions. In both cases, the system is allowed to relax until the total force acting on the system is less than 0.005 eV/\AA . At each pressure value, several different initial magnetic configurations were considered: (i) ferromagnetic (FM), (ii) zigzag antiferromagnetic (AFM), (iii) Néel AFM, (iv) stripy AFM, and (v) nonmagnetic (see Fig. 1).

The analysis of the electronic properties was done with the full-potential local orbital basis [26].

III. RESULTS AND DISCUSSION

A. Experimental results

The x-ray powder diffraction diagrams under pressure are displayed in Fig. 2. Additionally, we show the diffraction patterns at ambient pressure and at the highest studied pressure (25.2 GPa) together with the corresponding fits from the Rietveld refinement in Fig. 3. Both refinements were performed within the monoclinic unit cell with $C2/m$ symmetry. The same crystal symmetry is found for the closely related honeycomb iridates [4,27,28]. In the refinements, stacking

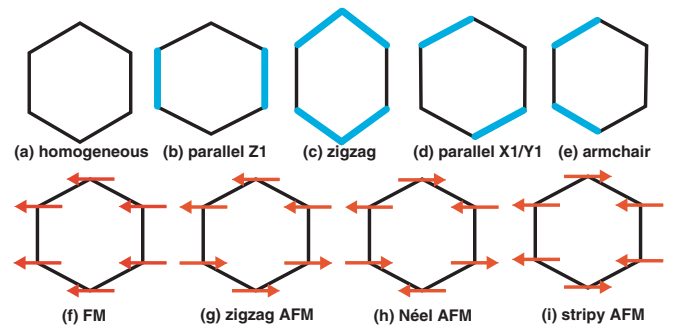


FIG. 1. Schematics of (a)–(e) various types of possible dimerization in hexagonal Kitaev systems and (f)–(i) different magnetic configurations considered by us for Li_2RhO_3 . The blue lines indicate the short bond l_s , i.e., the dimer, and the red arrows indicate the spin orientation at the transition-metal site.

faults associated with shifts between successive LiRh_2 layers were taken into account, as observed in $\alpha\text{-Li}_2\text{IrO}_3$ [27,28] and other Li_2MO_3 ($M = \text{Mn}, \text{Pt}, \text{Ru}$) compounds [27,29,30]. Stacking faults affect the intensity and line shape of several peaks and lead to an additional intensity between the (020) and (110) peaks, as marked by the dashed red arrows in the insets of Fig. 3. The presence of stacking faults was taken into account by introducing the Li/Rh mixing for the Rh(1)/Li(1) and Li(2)/Rh(2) sites while constraining the overall stoichiometry to Li_2RhO_3 . This reproduces the peak intensity but not its shape [27].

The lattice parameters as a function of pressure, as obtained by the Rietveld fits of the x-ray powder diffraction diagrams, are depicted in Fig. 4. Up to the critical pressure

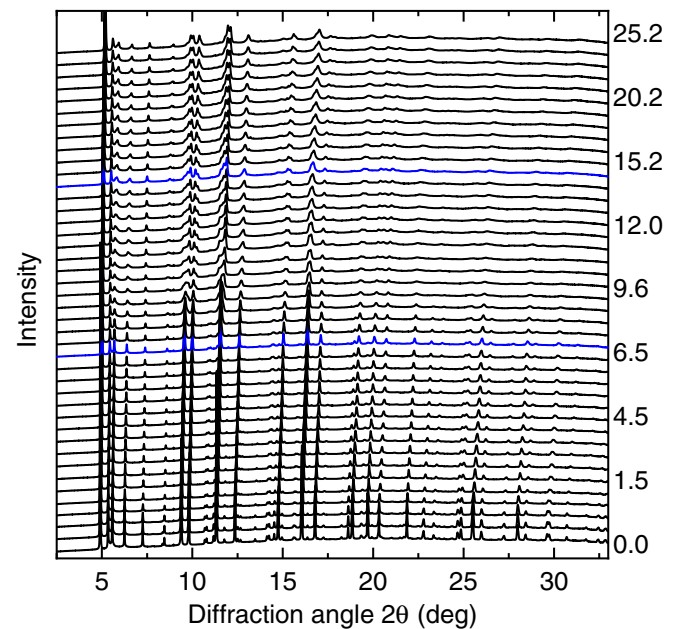


FIG. 2. Room-temperature x-ray powder diffraction diagrams of Li_2RhO_3 under pressure. The numbers on the right vertical axis denote the applied pressures in gigapascals. The diffraction diagrams at the critical pressures $P_{c1} = 6.5 \text{ GPa}$ and $P_{c2} = 14 \text{ GPa}$ are highlighted by blue lines.

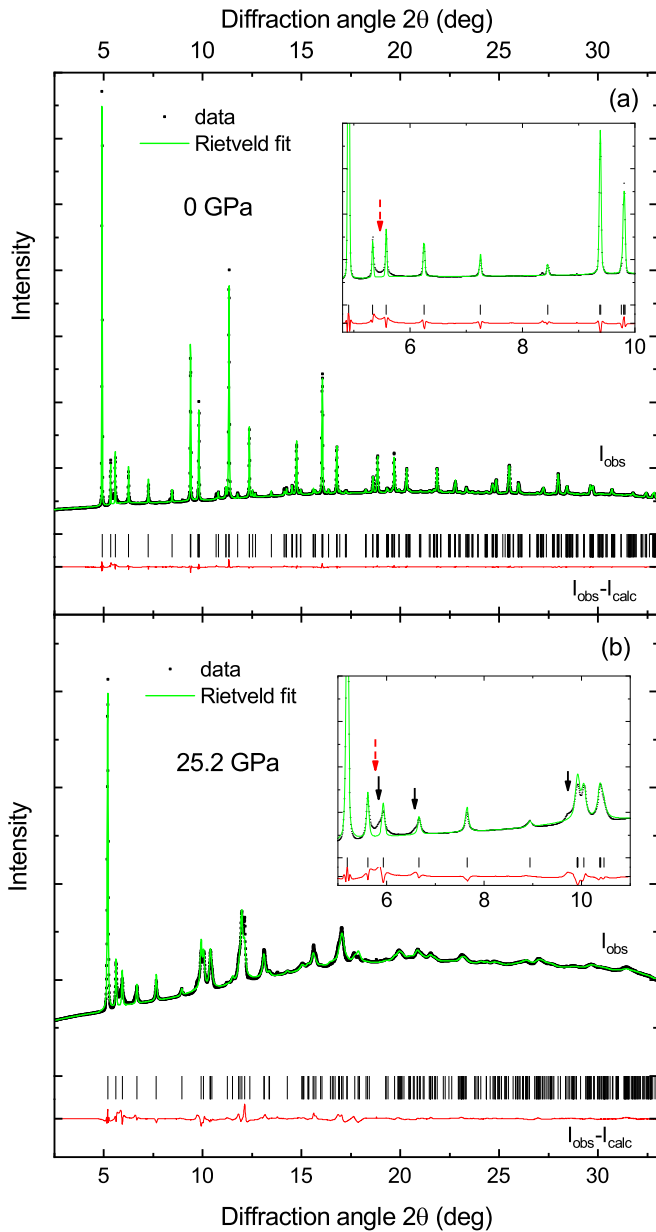


FIG. 3. X-ray powder diffraction diagrams I_{obs} of Li_2RhO_3 at (a) the ambient pressure and (b) the highest studied pressure (25.2 GPa) together with the corresponding Rietveld fits I_{calc} and the difference curves ($I_{obs} - I_{calc}$). Markers indicate the calculated peak positions. The R_p (R_{wp}) values amount to 6.31% (13.30%) and 6.15% (19.33%), respectively. The insets in (a) and (b) show the respective low-angle region at 0 and 25.2 GPa. The dashed red arrows in the insets mark the additional intensity due to stacking faults, while the black arrows in the inset of (b) mark traces from the low-pressure phase as discussed in the text.

$P_{c1} = 6.5$ GPa, the lattice parameters a , $b' = b/\sqrt{3}$, and c decrease monotonically with increasing pressure in a very similar manner. The c/a value, shown in the inset of Fig. 4(a), reveals that the strongest pressure-induced effect occurs for the lattice parameter c . The monoclinic angle β decreases slightly but monotonically within this pressure range.

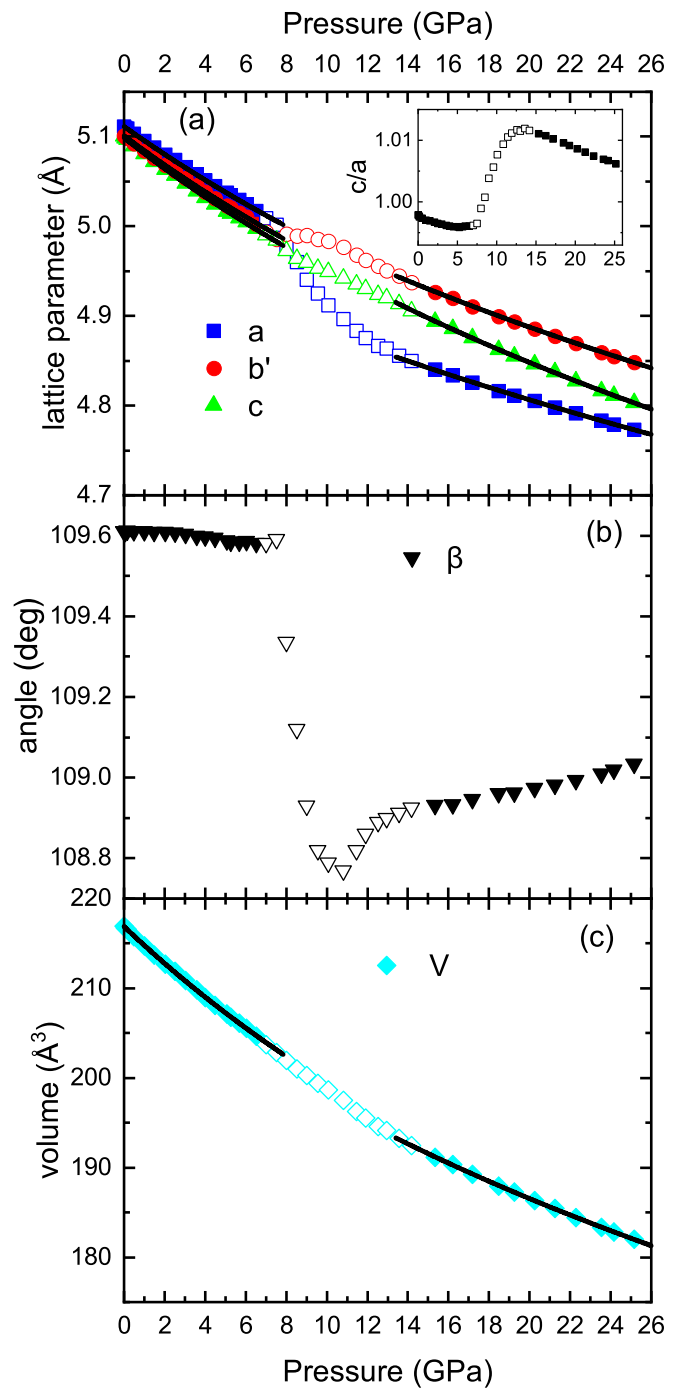


FIG. 4. Pressure evolution of (a) the lattice parameters (a , $b' = b/\sqrt{3}$, c) and c/a value (inset), (b) the monoclinic angle β and b/a value (inset, dashed line at $b/a = \sqrt{3}$), and (c) the volume V of the unit cell. The solid lines are fits with a Murnaghan equation of state as explained in the text. Open symbols mark the intermediate pressure regime, where the results may be less accurate due to the phase mixture (see text).

Above P_{c1} , a second phase with the same $C2/m$ symmetry appears and gets more pronounced with increasing pressure. The coexistence of two phases above P_{c1} suggests the first-order character of the phase transition. Above the critical pressure $P_{c2} = 14$ GPa, this second phase is dominant, and the

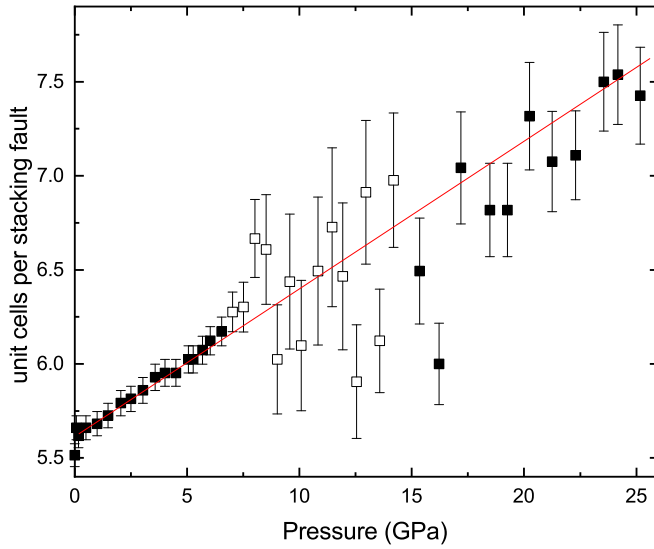


FIG. 5. Average number of unit cells per one stacking fault, as estimated from the fractional occupation of the Li(1)/Rh(1) site. The red line is a guide to the eye.

high-pressure diffractograms can be well described by a single phase with $C2/m$ symmetry. There are only traces of the low-pressure phase found in the diffraction patterns above P_{c2} and up to the highest studied pressure, marked with black arrows in the inset of Fig. 3(b). Most importantly, we can rule out a symmetry lowering above P_{c2} , as such a symmetry lowering would induce peak splittings, for example, for the (021) and the (111) diffraction peaks. These peaks are observed at 7.7° and 9.0° in the inset of Fig. 3(b) and are obviously not split. Thus, both the low-pressure ($P < P_{c1}$) and high-pressure ($P > P_{c2}$) phases in Li_2RhO_3 have $C2/m$ symmetry. This result is in contrast to the recent findings for $\alpha\text{-Li}_2\text{IrO}_3$, where a pressure-induced structural phase transition with symmetry lowering from monoclinic to triclinic symmetry caused by the Ir-Ir dimerization occurs at 3.8 GPa [15]. Analogously, the monoclinic to triclinic symmetry lowering with the Ru-Ru dimerization is observed in $\alpha\text{-RuCl}_3$ at $P \approx 1$ GPa [17].

The refinement of the diffraction patterns for the intermediate pressure range, $P_{c1} < P < P_{c2}$, with a phase mixture of the low-pressure and high-pressure phases did not yield stable fits, as many of the peaks of the two phases are broad and overlapping. Since the refinement with only one phase does not reproduce the actual peak shape, we marked this range with open symbols in Figs. 4, 5, 6, 7, and 8.

Between P_{c1} and P_{c2} , lattice parameter a decreases drastically by about 3%, while there is only a slight but abrupt increase in lattice parameter b , and c follows the pressure-induced monotonic decrease as observed below P_{c1} [see Fig. 4(a)]. The abrupt decrease in the a parameter is also revealed by the abrupt increase in the c/a ratio. Accordingly, the most pronounced pressure-induced change happens along the a lattice direction, as will be discussed in more detail later. The monoclinic angle β abruptly decreases above P_{c1} , and above P_{c2} it monotonically increases with increasing pressure [see Fig. 4(b)]. The kink in the pressure evolution of β in the pressure range 10–12 GPa, i.e., in the intermediate

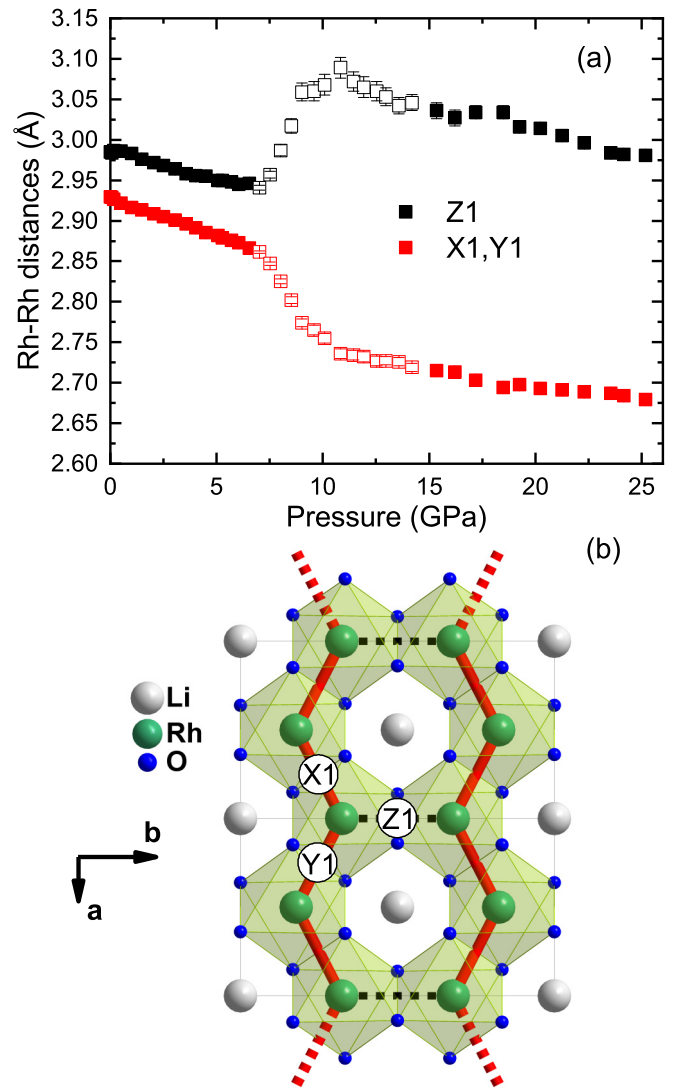


FIG. 6. (a) Rh-Rh bond lengths as a function of pressure for the rhodium hexagons in the ab plane with the nomenclature (Rh bonds X1, Y1, Z1) given in (b). The ratio l_1/l_s is calculated to ≈ 1.02 and ≈ 1.11 in the low- and high-pressure phases, respectively. The Rh zigzag chains along the X1 and Y1 bonds above P_{c2} are illustrated in (b) by thick red lines.

phase, is not discussed here because the phase mixture affects the refinements in this pressure range.

The pressure dependencies of the volume V and the lattice parameters r ($r = a, b, c$) were fitted separately for the low- and high-pressure phases, neglecting the intermediate regime, with a second-order Murnaghan equation of state (MOS) [31] to obtain the bulk moduli $B_{0,V}$ and $B_{0,r}$ according to

$$V(P) = V_0[(B'_{0,V}/B_{0,V})P + 1]^{-1/B'_{0,V}}, \quad (1)$$

$$r(P) = r_0[(B'_{0,r}/B_{0,r})P + 1]^{-1/3B'_{0,r}}, \quad (2)$$

with B' fixed to 4. The results are summarized in Table I. The bulk modulus $B_{0,V}$ of the low- and high-pressure phases amounts to 100.4(4) and 118.6(9) GPa, respectively. This means that the material is less compressible in the high-pressure phase. In the low-pressure phase ($P < P_{c1}$), the

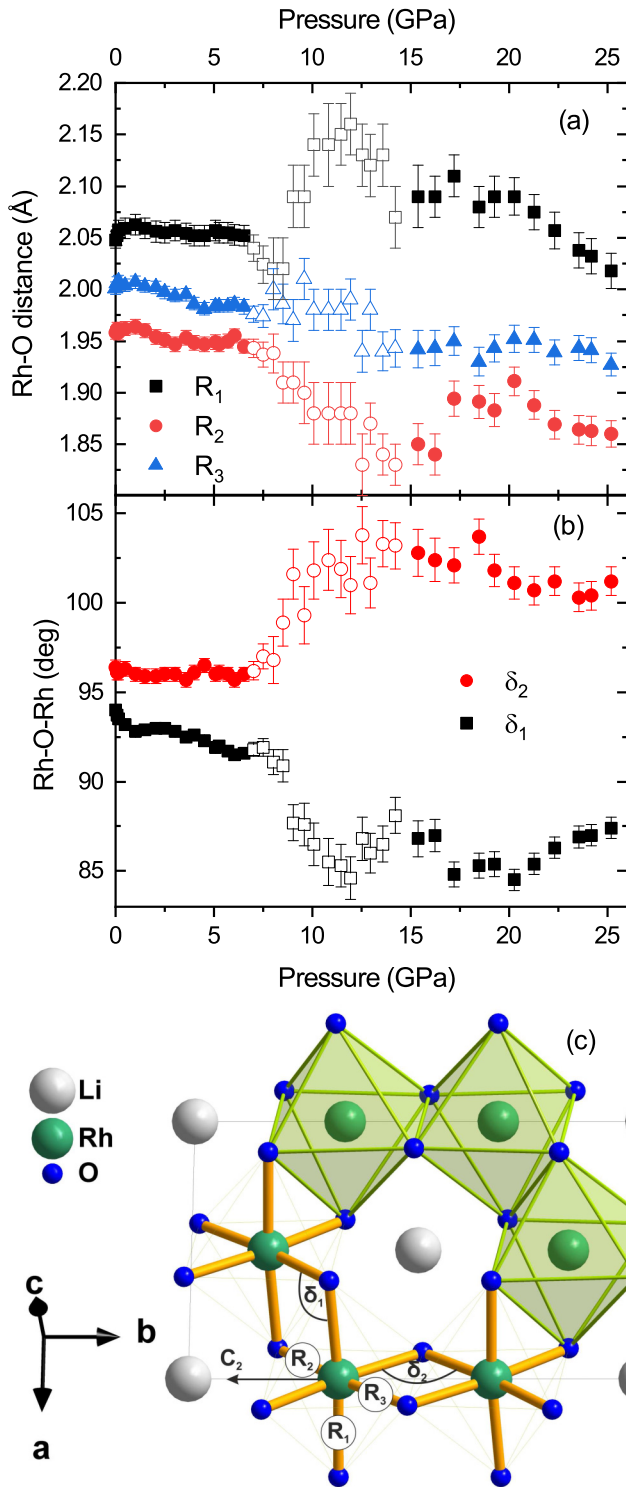


FIG. 7. Pressure dependence of the various octahedral (a) Rh-O distances (R_1 , R_2 , R_3) and (b) Rh-O-Rh bond angles (δ_1 , δ_2) with the nomenclature given in (c). The C_2 rotational axis is indicated by an arrow.

contribution of the c direction to the bulk modulus is the lowest, with $B_{0,c} = 94.8(7)$ GPa, as already indicated by the pressure dependence of the c/a ratio [inset of Fig. 4(a)]. Thus, the material is most compressible along the c direction. The

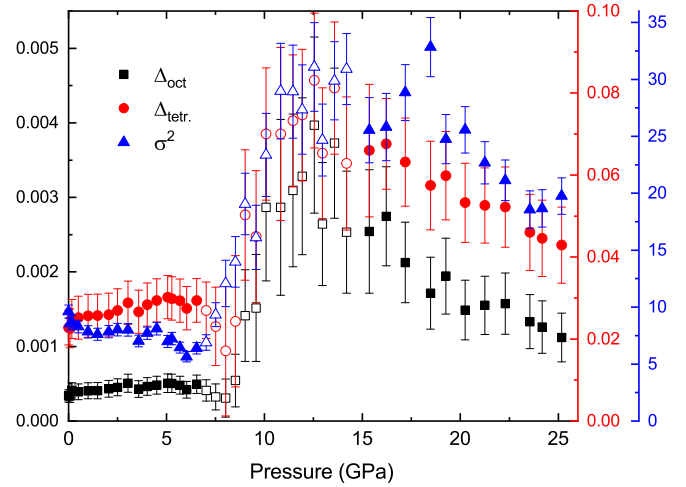


FIG. 8. Pressure dependence of the bond-length distortion Δ_{oct} , the tetragonal distortion Δ_{tetr} , and the bond-angle distortion σ_{oct}^2 as defined in the text.

largest contribution to the bulk modulus is attributed to the a crystal direction, with $B_{0,a} = 105.7(5)$ GPa.

In the high-pressure phase ($P > P_{c2}$), the contribution $B_{0,c}$ of the c direction remains low and is even slightly decreased compared to the low-pressure phase. Most interestingly, the contribution $B_{0,a}$ is strongly increased to 155.6(15) GPa in the high-pressure phase, while $B_{0,b}$ is much less increased, i.e., to 122.2(12) GPa. Hence, the honeycomb layers along the ab plane become less compressible in the high-pressure phase, whereby the pressure-induced hardening has the strongest effect along the a direction.

For a more detailed discussion, the atomic parameters of the refinement are shown in Table II. The partial exchange of Li and Rh accounts for the stacking faults, as described in Ref. [27]. Since three Rh atoms are required to change place with one Li atom in order to mimic one stacking fault and taking into account the site symmetry of the Rh(1) position (4g), the number of unit cells per stacking fault amounts to $3/(4\text{occ}_{\text{Li}(1)})$, where $\text{occ}_{\text{Li}(1)}$ denotes the Li(1) site occupancy. Accordingly, every 5.5(1) unit cells (along the c direction) one stacking fault occurs at ambient pressure. This value is very similar to previous reports on Li_2RhO_3 [8,32] and slightly higher than in $\alpha\text{-Li}_2\text{IrO}_3$ and Li_2PtO_3 [27]. On the other hand, different studies of Na_2IrO_3 [4,33] reported concentrations of stacking faults that are either larger or smaller than in

TABLE I. Bulk moduli $B_{0,v}$ and $B_{0,r}$, with $r = a, b, c$, in the low-pressure ($P < 6.5$ GPa) and high-pressure ($P > 14$ GPa) phases, as obtained from fitting the volume V and lattice parameters r with a MOS, with B'_0 set to 4.

	$P < 6.5$ GPa	$P > 15$ GPa
V_0 (Å ³)	216.90(3)	212.21(16)
$B_{0,v}$ (GPa)	100.4(4)	118.6(9)
$B_{0,a}$ (GPa)	105.7(5)	155.6(15)
$B_{0,b}$ (GPa)	100.2(6)	122.2(12)
$B_{0,c}$ (GPa)	94.8(7)	93.9(8)

TABLE II. Structural parameters for the low-pressure phase at ambient pressure and for the high-pressure phase at 25.2 GPa. At ambient pressure, the lattice parameters are $a = 5.11126(10) \text{ \AA}$, $b = 8.83473(16) \text{ \AA}$, $c = 5.10034(11) \text{ \AA}$, $\beta = 109.6105(18)^\circ$, and $V = 216.955(8) \text{ \AA}^3$, and at 25.2 GPa they are $a = 4.7732(5) \text{ \AA}$, $b = 8.3980(7) \text{ \AA}$, $c = 4.8027(3) \text{ \AA}$, $\beta = 109.034(11)^\circ$, and $V = 181.99(3) \text{ \AA}^3$. The isotropic atomic displacement parameters U_{iso} were fixed to 0.005 \AA^2 for all atomic positions, except for the Rh(1)/Li(1) one.

Atom	Site	Low-pressure phase (0 GPa)					High-pressure phase (25.2 GPa)				
		x	y	z	Occupancy	$U_{\text{iso}}(\text{\AA}^2)$	x	y	z	Occupancy	$U_{\text{iso}}(\text{\AA}^2)$
Rh(1)	4g	0	0.3311(2)	0	0.864(3)	0.0029(3)	0	0.3225(5)	0	0.899(7)	0.0047(11)
Li(1)	4g	0	0.3311(2)	0	0.136(3)	0.0029(3)	0	0.3225(5)	0	0.101(7)	0.0047(11)
Li(2)	2a	0	0	0	0.728(3)	0.005	0	0	0	0.798(7)	0.005
Rh(2)	2a	0	0	0	0.273(3)	0.005	0	0	0	0.202(7)	0.005
Li(3)	4h	0	0.820(3)	0.5	1	0.005	0	0.808(8)	0.5	1	0.005
Li(4)	2d	0	0.5	0.5	1	0.005	0	0.5	0.5	1	0.005
O(1)	8j	0.252(17)	0.3209(7)	0.7631(10)	1	0.005	0.271(3)	0.3332(16)	0.754(3)	1	0.005
O(2)	4i	0.274(2)	0	0.7726(19)	1	0.005	0.287(4)	0	0.774(4)	1	0.005

Li_2RhO_3 . The number of unit cells per stacking fault increases monotonically with increasing pressure and reaches 7.4(5) at 25.2 GPa, as shown in Fig. 5; that is, the number of stacking faults is slightly reduced by external pressure. The parameters for the oxygen positions are changed in the high-pressure phase compared to the low-pressure phase, thus affecting the RhO_6 octahedra. The most interesting change, however, is observed for the y parameter of Rh(1) that determines the Rh-Rh distances in the honeycomb network (see Table II).

To evaluate this behavior further, we compare the pressure evolution of the three Rh-Rh bond lengths in the ab plane, namely, the Z1 bond and the two degenerate X1/Y1 bonds, as depicted in Fig. 6(b). At ambient pressure, the Z1 bond length amounts to $2.985(3) \text{ \AA}$, while the X1/Y1 bond length is $2.9296(13) \text{ \AA}$ [see Fig. 6(a)], leading to a slightly distorted honeycomb. The corresponding bond disproportionation l_l/l_s , with l_l and l_s being the long and short bonds of the hexagonal Rh network, respectively, amounts to $l_l/l_s = 1.02$. For the high-pressure phase, both X1 and Y1 bonds are drastically reduced by $\approx 0.15 \text{ \AA}$, while the Z1 bond is increased by the same amount [Fig. 6(a)]. Hence, the bond disproportionation increased to $l_l/l_s = 1.11$ at 25 GPa. The X1/Y1 bond length of $\approx 2.7 \text{ \AA}$ above P_{c2} is close to but still larger than the interatomic distances in metallic rhodium ($d = 2.69 \text{ \AA}$ [34]). We thus conclude that external pressure introduces zigzag chains of rhodium atoms along the a direction, as illustrated in Fig. 6(b). A similar structure but with closer bond lengths is found for 5% Na-doped crystals $(\text{Li}_{0.95}\text{Na}_{0.05})_2\text{RuO}_3$ at ambient pressure [35]. On the other hand, pure Li_2RuO_3 is dimerized at ambient pressure with an armchair pattern of the short Ru-Ru bonds [see Fig. 1(e) for illustration] [35,36].

Next, we consider the pressure-induced changes in the RhO_6 octahedra. To this end, we define various Rh-O bond lengths and Rh-O-Rh bond angles that are responsible for the direct metal-to-metal and indirect oxygen-mediated contributions. The octahedra possess a twofold rotational C_2 axis which is indicated by the arrow in Fig. 7(c). There are three unique Rh-O bonds labeled R_1 , R_2 , R_3 and two unique Rh-O-Rh angles δ_1 and δ_2 , where δ_1 (δ_2) involves two Rh atoms connected via the X1/Y1 bond (Z1 bond) [see Fig. 7(c)]. The pressure dependence of the various bonds and bond angles is depicted in Figs. 7(a) and 7(b), respectively. At

ambient pressure, the largest Rh-O bond length is found for the apical oxygen atom; thus, the RhO_6 octahedra show a tetragonal distortion with axial elongation. In the low-pressure phase ($P < P_{c1}$), the bond length R_1 is pressure independent, whereas R_2 and R_3 slightly decrease under pressure.

At P_{c2} , the length R_1 is increased compared to the low-pressure phase, whereas R_2 and R_3 are decreased. Upon further compression, R_1 decreases, R_3 seems to be unaffected, and R_2 shows a small anomaly at 15–20 GPa that may be significant, as the changes exceed the error bars.

The formation of zigzag chains is predominantly due to a change in Rh-O-Rh angles as described in the following. The pressure dependence of the Rh-O-Rh bond angles δ_1 and δ_2 is shown in Fig. 7(b). At ambient pressure, the values of δ_1 and δ_2 amount to $94.0(3)^\circ$ and $96.4(4)^\circ$, respectively. While δ_2 is independent of pressure in the low-pressure phase, δ_1 decreases by increasing pressure. When entering the high-pressure phase above P_{c2} the bond angle δ_1 is strongly decreased to the value 87° . Interestingly, the onset of the intermediate phase at P_{c1} appears at a pressure when δ_1 approaches 90° , which is a distinct angle for the contributions of the ligand-mediated hopping to the hopping parameters, as discussed in more detail in Refs. [7,37]. The strong pressure-induced decrease in the angle δ_1 between P_{c1} and P_{c2} confirms the formation of Rh zigzag chains along the a direction. Consistently, the bond angle δ_2 is strongly increased, as the Z1 bond length is increased [see Fig. 6(a)]. Again, an anomaly is observed for the Rh-O-Rh bond angles between 15 and 20 GPa, which is directly related to the anomaly for the Rh-O distances and thereby has the same origin.

The electronic states of Li_2RhO_3 are affected by the distortion of the RhO_6 octahedra. Therefore, we followed the pressure dependence of the octahedral distortion using the bond-length distortion Δ_{oct} and the bond-angle distortion σ_{oct}^2 [38–40]. The bond-length distortion is defined as $\Delta_{\text{oct}} = \frac{1}{6} \sum_{i=1}^6 [(d_i - d_{\text{av}})/d_{\text{av}}]^2$, where d_i is an individual Rh-O bond length and d_{av} is the average Rh-O bond length in the RhO_6 octahedron. The bond-angle distortion is calculated according to $\sigma_{\text{oct}}^2 = \frac{1}{11} \sum_{i=1}^{12} (\alpha_i - 90)^\circ^2$, where α_i is an individual O-Rh-O bond angle. At ambient pressure, the distortion parameters are $\Delta_{\text{oct}} = 3.4(11) \times 10^{-4}$ and $\sigma^2 = 9.6(6)$, comparable to the results in Ref. [32] [$\Delta_{\text{oct}} = 1.2(6) \times 10^{-4}$ and

$\sigma^2 = 9.6(5)$], although the Rh position seems to be fixed in that report. Comparison of our refinement to previous ones [8,14] is not straightforward since in those studies some oxygen parameters were fixed or calculated. The distortion parameters for Li_2RhO_3 reported in our study are comparable to the ones of the related materials $\alpha\text{-Li}_2\text{IrO}_3$ and Li_2PtO_3 [27,28]. For Na_2IrO_3 the Δ_{oct} value is about one magnitude smaller, while the bond-angle distortion σ^2 is nearly doubled [4,33]. A comparison to the octahedral distortions in dimerized Li_2RuO_3 is difficult since the reported values determined by various studies are not consistent. For example, the Δ_{oct} values between 1.4×10^{-4} and 24×10^{-4} have been reported, and the values for σ^2 range between 4.7 and 54 [35,41,42].

In the low-pressure phase, the bond-length distortion only slightly increases with increasing pressure, whereas the bond-angle distortion decreases (Fig. 8). At the critical pressure P_{c2} , both parameters Δ_{oct} and σ_{oct}^2 are drastically enhanced compared to the low-pressure range. Such an enhanced distortion was also reported in Ref. [41] for dimerized Li_2RuO_3 compared to the nondimerized samples. It is therefore likely that the enhancement of Δ_{oct} and σ_{oct}^2 at P_{c2} is caused by the lattice strain due to the formation of the Rh-Rh zigzag chains in Li_2RhO_3 .

Of further interest is the tetragonal distortion (elongation or compression along the z direction) of the octahedra, as this would cause a splitting of the Rh t_{2g} states. As a measure of the tetragonal distortion we define the parameter Δ_{tet} as the deviation of the apical Rh-O bond length R_1 from the average Rh-O bond length d_{av} according to $\Delta_{\text{tet}} = (R_1 - d_{\text{av}})/d_{\text{av}}$ [39]. For positive (negative) nonzero values of Δ_{tet} the octahedra are elongated (compressed) along the apical bond direction. Such a distortion can be explained by a cooperative first-order Jahn-Teller effect neglecting stress on the system [43,44]. The Jahn-Teller effect is expected to be weak but nonzero in a d^5 configuration. The pressure dependence of Δ_{tet} is depicted in Fig. 8. We note that the tetragonal distortion at ambient pressure amounts to $\Delta_{\text{tet}} = 0.023(4)$, which is comparable to the value $\Delta_{\text{tet}} = 0.015(3)$ given in Ref. [32]. In the low-pressure phase, Δ_{tet} increases slightly but steadily upon compression; that is, the elongation increases.

Between the low- and high-pressure phases, Δ_{tet} is nearly doubled, before it decreases upon further compression above P_{c2} . While the tetragonal distortion in the low-pressure phase is comparable to that in Li_2MO_3 ($M = \text{Ir}, \text{Pt}$), it is much more pronounced than in Na_2IrO_3 , where Δ_{tet} is close to zero. We thus conclude that the lattice strain rather than the Jahn-Teller effect is the driving force for the distortion of the octahedra in the honeycomb lattices. The tetragonal distortion in the high-pressure phase of Li_2RhO_3 is comparable to the tetragonal distortion in the perovskites Sr_2RhO_4 and Sr_2RuO_4 , where the bond angle distortion is zero [45,46].

B. Computational results

A question that remains open is why Li_2RhO_3 retains the monoclinic $C2/m$ symmetry and shows the zigzag-chain pattern of short Rh-Rh bonds under pressure, whereas $\alpha\text{-Li}_2\text{IrO}_3$ [15,16] and $\alpha\text{-RuCl}_3$ [17] become triclinic following the formation of metal-metal dimers.

In previous studies, the experimentally observed dimerization pattern in $\alpha\text{-Li}_2\text{IrO}_3$ and $\alpha\text{-RuCl}_3$ was identified by DFT calculations within the GGA+SOC+ U scheme [15] as a consequence of a complex interplay of SOC, magnetism, correlation, and covalent bonding. Following this knowledge, we performed full relaxations of Li_2RhO_3 as a function of hydrostatic pressure with and without SOC. As an initial guess for the geometrical optimization at each pressure, we considered two structures: the experimental low-pressure “undistorted” structure at 5 GPa and the experimental high-pressure “zigzag chain” structure at 25.2 GPa. In our notation, we assume a structure is undistorted when the corresponding bond disproportionation $l_l/l_s < 1.04$. Moreover, for each of these initial geometries, we considered five different spin configurations, as explained in Sec. II B.

Test calculations performed at 25 GPa reveal that after relaxation the structure becomes dimerized, regardless of the initial configuration. At a given pressure, the energetics of the various different configurations are obtained by comparing the corresponding enthalpies. Due to the underbinding problem of GGA (relaxed interatomic distances are longer than their experimental counterparts), the volume corresponding to 2 GPa reproduces the experimental volume at ambient pressure. This has been corrected by systematically subtracting $\Delta P = 2$ GPa from all simulated pressure values.

The value of Hubbard correlation $U = 1.5$ eV was chosen such that at 5 GPa (within the GGA+SOC+ U scheme) (i) the optimized lowest-enthalpy magnetic configuration corresponds to $C2/m$ symmetry and reproduces the experimental value of $l_l/l_s = 1.02$ and (ii) the nonmagnetic configuration is dimerized (though the parallel $X1/Y1$ type). The latter confirms dimerization at finite pressure for Li_2RhO_3 as magnetism is known to work against dimerization by pushing the transition pressure to a higher value [15].

At a pressure $P_c^{\text{noSOC}} \approx 11$ GPa, we find that Li_2RhO_3 undergoes a phase transition from a homogeneous to a dimerized phase with bond disproportionation $l_l/l_s = 1.146$ within the GGA+ U scheme (not shown here). Upon dimerization, Li_2RhO_3 becomes nonmagnetic. However, there are a few discrepancies with the experimental structures: (i) below P_c^{noSOC} , in the homogeneous structure, the shorter bond corresponds to the $Z1$ bond, rather than to the $X1$ and $Y1$ bonds as observed in experiments, and (ii) the dimerized phase does not have $C2/m$ symmetry; rather, it has triclinic ($P\bar{1}$) symmetry, similar to $\alpha\text{-RuCl}_3$ [17] and $\alpha\text{-Li}_2\text{IrO}_3$ [15,16]. The inclusion of SOC causes the shorter bond to be $X1/Y1$ in the homogeneous phase (below P_c^{SOC}) and shifts the transition pressure P_{cm} to 27 GPa. However, the high-pressure structure still becomes triclinic with $l_l/l_s = 1.15$ (see Fig. 9).

The above results show that the experimental zigzag pattern of the short Rh-Rh bonds cannot be obtained from hydrostatic pressure simulations. We therefore proceed by simulating uniaxial pressure with the b and c parameters fixed to their experimental values at 25.5 GPa and the b/a ratio varied systematically (Fig. 10). This approach yields the zigzag-chain structure observed experimentally. However, we had to increase the b/a ratio to 1.95 in order to reproduce the ratio l_l/l_s between the long and short bonds.

To obtain the pressure evolution of Rh-Rh bonds under uniaxial condition, we next repeated the above calculations but

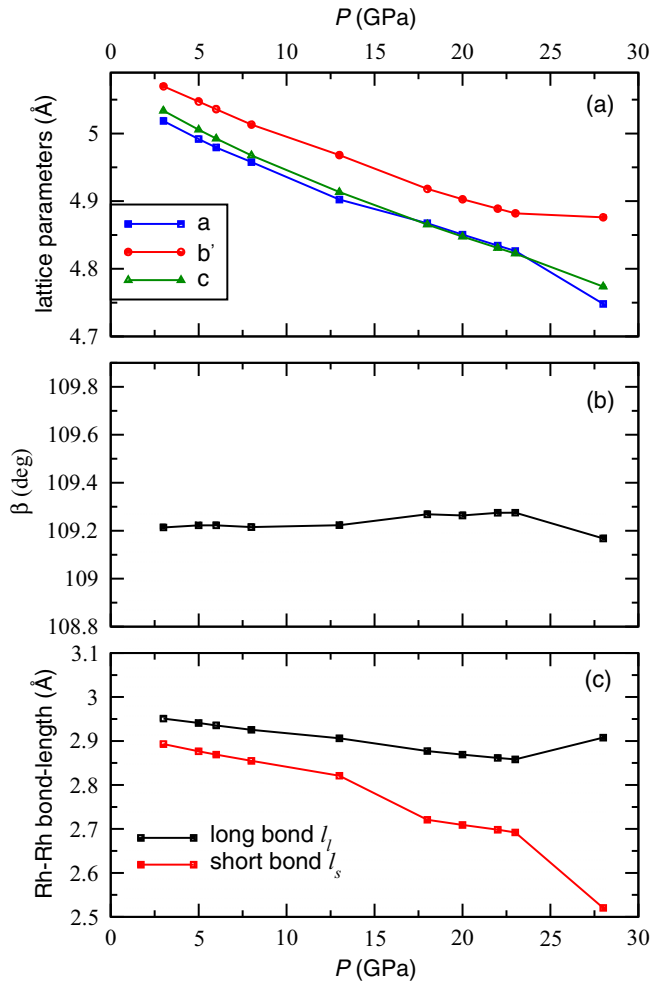


FIG. 9. Pressure dependence of the theoretically obtained (a) and (b) structural parameters calculated under hydrostatic pressure conditions and (c) Rh-Rh bond lengths within the GGA+SOC+ U ($U = 1.5$ eV) scheme.

this time with $b/a = 1.95$ while fixing the b and c parameters to their experimental values at the corresponding pressure. By comparing the results of the hydrostatic and uniaxial pressure simulations, we conclude (see Fig. 11) that the evolution of Li_2RhO_3 up to P_{c1} is compatible with hydrostatic pressure conditions, whereas at higher pressures the system progressively moves toward the behavior expected under uniaxial pressure. The uniaxial pressure accounts for the formation of zigzag chains instead of dimers, although it does not fully account for the evolution of the longer Rh-Rh bonds that evolve smoothly in the simulation but show a steplike anomaly experimentally (Fig. 6).

At ambient conditions, Li_2RhO_3 is an insulator, as shown in Ref. [14]. Our calculated density of states (DOS) for the experimentally obtained structures at 25.2 GPa (Fig. 12) show that unlike other dimerized phases in $\alpha\text{-Li}_2\text{IrO}_3$ and $\alpha\text{-RuCl}_3$, in Li_2RhO_3 the degeneracy between yz and xz orbitals of Rh d states does not get lifted as the symmetry remains the same. Moreover, the system probably becomes metallic under pressure due to the formation of zigzag chains, which provide new hopping pathways.

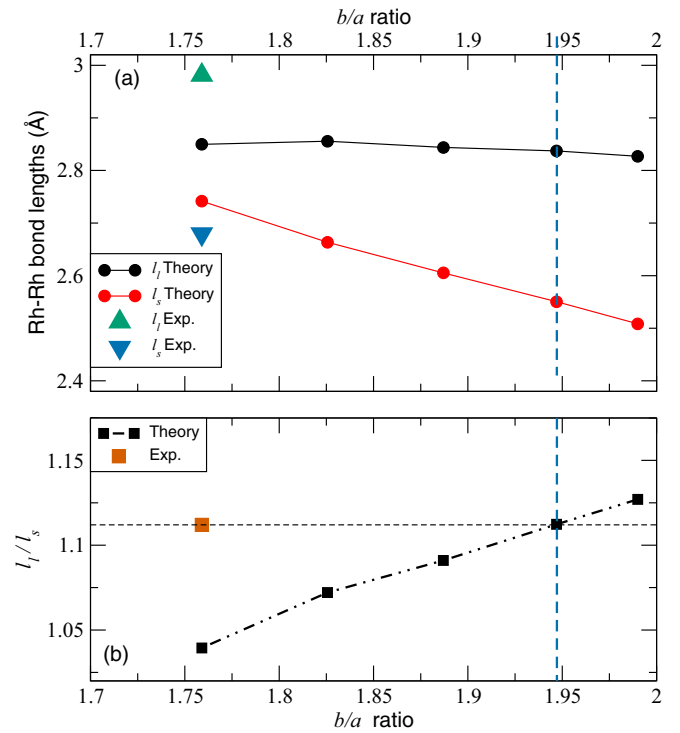


FIG. 10. Variation of (a) the Rh-Rh bond lengths and (b) bond disproportionation (l_l/l_s) as a function of the b/a ratio, with the b and c parameters fixed to their experimental values at 25.2 GPa (within GGA+SOC+ U), and comparison with experimentally obtained values. The dashed blue lines show the optimal value of the b/a ratio that illustrates the choice of lattice parameters for uniaxial pressure conditions in the simulation.

The origin of the uniaxial-like pressure conditions requires further investigation. Experimental pressure conditions in a DAC with helium as the pressure-transmitting medium are

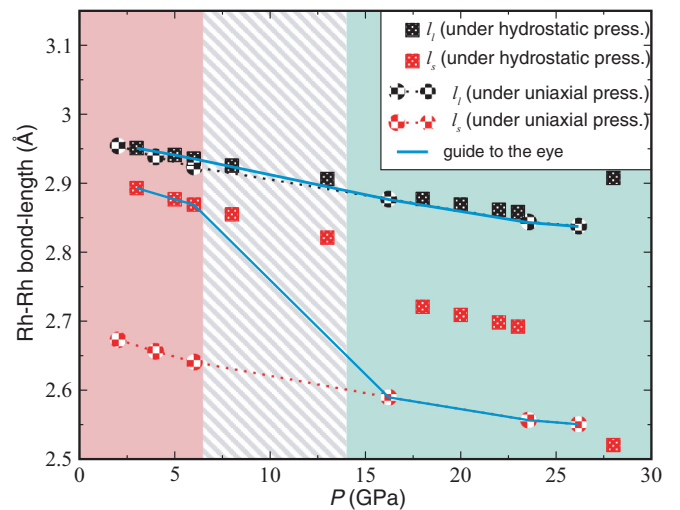


FIG. 11. The evolution of Rh-Rh bond lengths (calculated within GGA+SOC+ U) as a function of pressure. Red and green shaded regions represent hydrostatic and uniaxial pressure regimes, respectively. For comparison with the experimental data, the blue line is drawn as a guide to follow the transition from hydrostatic to uniaxial pressure.

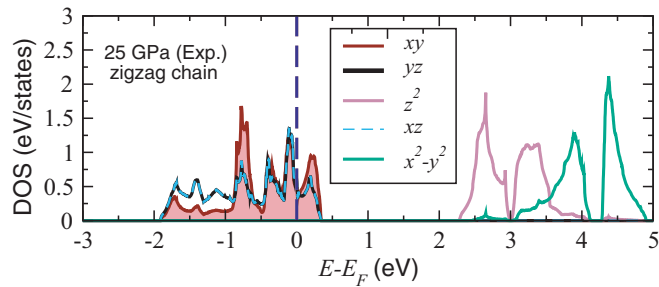


FIG. 12. Orbital-projected DOS for the Rh d orbitals in the experimental structure with $C2/m$ symmetry at 25.5 GPa, calculated within the GGA+SOC+ U scheme with $U = 1.5$ eV.

expected to be hydrostatic [47]. Therefore, we consider the nature of the Li_2RhO_3 sample as a more plausible reason. In particular, stacking faults that occur, on average, every six to seven layers could act as a local strain and affect the evolution of the structure under pressure. Our data show that the concentration of stacking faults in Li_2RhO_3 is higher than in the polycrystalline samples of $\alpha\text{-Li}_2\text{IrO}_3$ and in single crystals of $\alpha\text{-Li}_2\text{IrO}_3$ that were used in our previous study [15]. Interestingly, Na_2IrO_3 shows different pressure evolutions of the crystal structure in powders [48] and single crystals [49]. Given the proclivity of Na_2IrO_3 for the formation of stacking faults, a similar mechanism may be operative there and deserves further systematic investigation.

IV. CONCLUSION

In contrast to $\alpha\text{-Li}_2\text{IrO}_3$ and $\alpha\text{-RuCl}_3$, where a dimerized triclinic phase is stabilized under pressure, Li_2RhO_3 retains its ambient-pressure monoclinic $C2/m$ symmetry and develops zigzag chains of short Rh-Rh bonds. This structural phase transition is not abrupt since traces of the low-pressure phase can still be found even at the highest pressure of 25.2 GPa, but above ≈ 14 GPa the high-pressure phase is dominant. Our density-functional calculations suggest that such a behavior is not anticipated in Li_2RhO_3 under hydrostatic pressure, where conventional dimerization should occur. On the other hand, uniaxial pressure may explain the experimental observations and promote the formation of zigzag chains instead of dimers.

ACKNOWLEDGMENTS

We thank the ESRF, Grenoble, for the provision of beam time at ID15B. D.K., R.V., A.A.T., and P.G. acknowledge financial support from the Deutsche Forschungsgemeinschaft (DFG), Germany, through TRR 80 (Project No. 107745057), SPP 1666 (Project No. 220179758), TRR 49 (Project No. 31867626), and SFB 1238 (Project No. 277146847). A.J. acknowledges support from the DFG through Grant No. JE 748/1. S.B. thanks S. Winter for helpful discussions. A.A.T. acknowledges financial support from the Federal Ministry for Education and Research via the Sofja-Kovalevskaya Award of the Alexander von Humboldt Foundation, Germany.

- [1] A. Kitaev, Anyons in an exactly solved model and beyond, *Ann. Phys. (NY)* **321**, 2 (2006).
- [2] G. Jackeli and G. Khaliullin, Mott Insulators in the Strong Spin-Orbit Coupling Limit: From Heisenberg to a Quantum Compass and Kitaev Models, *Phys. Rev. Lett.* **102**, 017205 (2009).
- [3] J. Chaloupka, G. Jackeli, and G. Khaliullin, Kitaev-Heisenberg Model on a Honeycomb Lattice: Possible Exotic Phases in Iridium Oxides A_2IrO_3 , *Phys. Rev. Lett.* **105**, 027204 (2010).
- [4] S. K. Choi, R. Coldea, A. N. Kolmogorov, T. Lancaster, I. I. Mazin, S. J. Blundell, P. G. Radaelli, Y. Singh, P. Gegenwart, K. R. Choi, S.-W. Cheong, P. J. Baker, C. Stock, and J. Taylor, Spin Waves and Revised Crystal Structure of Honeycomb Iridate Na_2IrO_3 , *Phys. Rev. Lett.* **108**, 127204 (2012).
- [5] K. W. Plumb, J. P. Clancy, L. J. Sandilands, V. V. Shankar, Y. F. Hu, K. S. Burch, H.-Y. Kee, and Y.-J. Kim, $\alpha\text{-RuCl}_3$: A spin-orbit assisted Mott insulator on a honeycomb lattice, *Phys. Rev. B* **90**, 041112(R) (2014).
- [6] S. H. Chun, J.-W. Kim, J. Kim, H. Zheng, C. C. Stoumpos, C. D. Malliakas, J. F. Mitchell, K. Mehlawat, Y. Singh, Y. Choi, T. Gog, A. Al-Zein, M. M. Sala, M. Krisch, J. Chaloupka, G. Jackeli, G. Khaliullin, and B. J. Kim, Direct evidence for dominant bond-directional interactions in a honeycomb lattice iridate Na_2IrO_3 , *Nat. Phys.* **11**, 462 (2015).
- [7] S. M. Winter, A. A. Tsirlin, M. Daghofer, J. van den Brink, Y. Singh, P. Gegenwart, and R. Valentí, Models and materials for generalized Kitaev magnetism, *J. Phys.: Condens. Matter* **29**, 493002 (2017).
- [8] Y. Luo, C. Cao, B. Si, Y. Li, J. Bao, H. Guo, X. Yang, C. Shen, C. Feng, J. Dai, G. Cao, and Z.-an Xu, Li_2RhO_3 : A spin-glassy relativistic Mott insulator, *Phys. Rev. B* **87**, 161121(R) (2013).
- [9] P. Khuntia, S. Manni, F. R. Foronda, T. Lancaster, S. J. Blundell, P. Gegenwart, and M. Baenitz, Local magnetism and spin dynamics of the frustrated honeycomb rhodate Li_2RhO_3 , *Phys. Rev. B* **96**, 094432 (2017).
- [10] J. A. Sears, M. Songvilay, K. W. Plumb, J. P. Clancy, Y. Qiu, Y. Zhao, D. Parshall, and Y.-J. Kim, Magnetic order in $\alpha\text{-RuCl}_3$: A honeycomb-lattice quantum magnet with strong spin-orbit coupling, *Phys. Rev. B* **91**, 144420 (2015).
- [11] A. Banerjee, C. A. Bridges, J.-Q. Yan, A. A. Aczel, L. Li, M. B. Stone, G. E. Granroth, M. D. Lumsden, Y. Yiu, J. Knolle, S. Bhattacharjee, D. L. Kovrizhin, R. Moessner, D. A. Tennant, D. G. Mandrus, and S. E. Nagler, Proximate Kitaev quantum spin liquid behavior in a honeycomb magnet, *Nat. Mater.* **15**, 733 (2016).
- [12] S. C. Williams, R. D. Johnson, F. Freund, S. Choi, A. Jesche, I. Kimchi, S. Manni, A. Bombardi, P. Manuel, P. Gegenwart, and R. Coldea, Incommensurate counterrotating magnetic order stabilized by Kitaev interactions in the layered honeycomb $\alpha\text{-Li}_2\text{IrO}_3$, *Phys. Rev. B* **93**, 195158 (2016).
- [13] V. M. Katakuri, S. Nishimoto, I. Rousochatzakis, H. Stoll, J. van den Brink, and L. Hozoi, Strong magnetic frustration and anti-site disorder causing spin-glass behavior in honeycomb Li_2RhO_3 , *Sci. Rep.* **5**, 14718 (2015).

- [14] I. I. Mazin, S. Manni, K. Foyevtsova, H. O. Jeschke, P. Gegenwart, and R. Valentí, Origin of the insulating state in honeycomb iridates and rhodates, *Phys. Rev. B* **88**, 035115 (2013).
- [15] V. Hermann, M. Altmeyer, J. Ebad-Allah, F. Freund, A. Jesche, A. A. Tsirlin, M. Hanfland, P. Gegenwart, I. I. Mazin, D. I. Khomskii, R. Valentí, and C. A. Kuntscher, Competition between spin-orbit coupling, magnetism, and dimerization in the honeycomb iridates: α -Li₂IrO₃ under pressure, *Phys. Rev. B* **97**, 020104(R) (2018).
- [16] J. P. Clancy, H. Gretarsson, J. A. Sears, Y. Singh, S. Desgreniers, K. Mehlatat, S. Layek, G. Kh. Rozenberg, Y. Ding, M. H. Upton, D. Casa, N. Chen, J. Im, Y. Lee, R. Yadav, L. Hozoi, D. Efremov, J. van den Brink, and Y.-J. Kim, Pressure-driven collapse of the relativistic electronic ground state in a honeycomb iridate, *npj Quantum Mater.* **3**, 35 (2018).
- [17] G. Bastien, G. Garbarino, R. Yadav, F. J. Martinez-Casado, R. Beltrán Rodríguez, Q. Stahl, M. Kusch, S. P. Limandri, R. Ray, P. Lampen-Kelley, D. G. Mandrus, S. E. Nagler, M. Roslova, A. Isaeva, T. Doert, L. Hozoi, A. U. B. Wolter, B. Büchner, J. Geck, and J. van den Brink, Pressure-induced dimerization and valence bond crystal formation in the Kitaev-Heisenberg magnet α -RuCl₃, *Phys. Rev. B* **97**, 241108(R) (2018).
- [18] T. Biesner, S. Biswas, W. Li, Y. Saito, A. Pustogow, M. Altmeyer, A. U. B. Wolter, B. Büchner, M. Roslova, T. Doert, S. M. Winter, R. Valentí, and M. Dressel, Detuning the honeycomb of α -RuCl₃: Pressure-dependent optical studies reveal broken symmetry, *Phys. Rev. B* **97**, 220401(R) (2018).
- [19] S. Manni, Synthesis and investigation of frustrated Honeycomb lattice iridates and rhodates, Ph.D. thesis, University of Goettingen, 2014.
- [20] V. Petříček, M. Dušek, and L. Palatinus, Crystallographic Computing System JANA2006: General features, *Z. Kristallogr. – Cryst. Mater.* **229**, 345 (2014).
- [21] R. A. Young, *The Rietveld Method*, reprint, International Union of Crystallography Monographs on Crystallography Vol. 5 (Oxford University Press, Oxford, 2002).
- [22] R. B. Von Dreele, M. R. Suchoamel, and B. H. Toby, Compute X-ray Absorption, Argonne National Laboratory (2013), <https://11bm.xray.aps.anl.gov/absorb/absorb.php>.
- [23] P. E. Blöchl, Projector augmented-wave method, *Phys. Rev. B* **50**, 17953 (1994).
- [24] G. Kresse and J. Hafner, *Ab initio* molecular dynamics for liquid metals, *Phys. Rev. B* **47**, 558 (1993).
- [25] S. L. Dudarev, G. A. Botton, S. Y. Savrasov, C. J. Humphreys, and A. P. Sutton, Electron-energy-loss spectra and the structural stability of nickel oxide: An LSDA+*U* study, *Phys. Rev. B* **57**, 1505 (1998).
- [26] K. Koepnick and H. Eschrig, Full-potential nonorthogonal local-orbital minimum-basis band-structure scheme, *Phys. Rev. B* **59**, 1743 (1999).
- [27] M. J. O'Malley, H. Verweij, and P. M. Woodward, Structure and properties of ordered Li₂IrO₃ and Li₂PtO₃, *J. Solid State Chem.* **181**, 1803 (2008).
- [28] F. Freund, S. C. Williams, R. D. Johnson, R. Coldea, P. Gegenwart, and A. Jesche, Single crystal growth from separated educts and its application to lithium transition-metal oxides, *Sci. Rep.* **6**, 35362 (2016).
- [29] J. Bréger, M. Jiang, N. Dupré, Y. S. Meng, Y. Shao-Horn, G. Ceder, and C. P. Grey, High-resolution X-ray diffraction, DIFFaX, NMR and first principles study of disorder in the Li₂MnO₃-Li[Ni_{1/2}Mn_{1/2}]O₂ solid solution, *J. Solid State Chem.* **178**, 2575 (2005).
- [30] M. Casas-Cabanas, J. Rodríguez-Carvajal, J. Canales-Vázquez, Y. Laligant, P. Lacorre, and M. R. Palacín, Microstructural characterisation of battery materials using powder diffraction data: DIFFaX, FAULTS and SH-FullProf approaches, *J. Power Sources* **174**, 414 (2007).
- [31] F. D. Murnaghan, The Compressibility of Media under Extreme Pressures, *Proc. Natl. Acad. Sci. USA* **30**, 244 (1944).
- [32] V. Todorova and M. Jansen, Synthesis, Structural Characterization and Physical Properties of a New Member of Ternary Lithium Layered Compounds - Li₂RhO₃, *Z. Anorg. Allg. Chem.* **637**, 37 (2011).
- [33] F. Ye, S. Chi, H. Cao, B. C. Chakoumakos, J. A. Fernandez-Baca, R. Custelcean, T. F. Qi, O. B. Korneta, and G. Cao, Direct evidence of a zigzag spin-chain structure in the honeycomb lattice: A neutron and x-ray diffraction investigation of single-crystal Na₂IrO₃, *Phys. Rev. B* **85**, 180403(R) (2012).
- [34] E. S. Bale, The Structure of Rhodium, *Platinum Metals Rev.* **2**, 61 (1958).
- [35] K. Mehlatat and Y. Singh, First-order magnetostructural transition in single crystals of the honeycomb lattice ruthenate Li₂RuO₃, *Phys. Rev. B* **95**, 075105 (2017).
- [36] S. A. J. Kimber, I. I. Mazin, J. Shen, H. O. Jeschke, S. V. Streltsov, D. N. Argyriou, R. Valentí, and D. I. Khomskii, Valence bond liquid phase in the honeycomb lattice material Li₂RuO₃, *Phys. Rev. B* **89**, 081408(R) (2014).
- [37] S. M. Winter, Y. Li, H. O. Jeschke, and R. Valentí, Challenges in design of Kitaev materials: Magnetic interactions from competing energy scales, *Phys. Rev. B* **93**, 214431 (2016).
- [38] A. Ertl, J. M. Hughes, F. Pertlik, F. F. Foit, S. E. Wright, F. Brandstatter, and B. Marler, Polyhedron distortions in tourmaline, *Can. Mineral.* **40**, 153 (2002).
- [39] E. S. Kim, S. H. Kim, and K. H. Yoon, Dependence of Thermal Stability on Octahedral Distortion of (1 - x)(Ca_{0.3}Li_{0.119}Sm_{0.427})TiO_{3-x}LnAlO₃ (Ln = Nd, Sm) Ceramics, *J. Ceram. Soc. Jpn. Supplement* **112**, S1645 (2004).
- [40] T. Hogan, X. Wang, H. Chu, D. Hsieh, and S. D. Wilson, Doping-driven structural distortion in the bilayer iridate (Sr_{1-x}La_x)₃Ir₂O₇, *Phys. Rev. B* **95**, 174109 (2017).
- [41] J. C. Wang, J. Terzic, T. F. Qi, F. Ye, S. J. Yuan, S. Aswartham, S. V. Streltsov, D. I. Khomskii, R. K. Kaul, and G. Cao, Lattice-tuned magnetism of Ru⁴⁺ (4d⁴) ions in single crystals of the layered honeycomb ruthenates Li₂RuO₃ and Na₂RuO₃, *Phys. Rev. B* **90**, 161110(R) (2014).
- [42] H. Kobayashi, R. Kanno, Y. Kawamoto, M. Tabuchi, O. Nakamura, and M. Takano, Structure and lithium deintercalation of Li_{2-x}RuO₃, *Solid State Ionics* **82**, 25 (1995).
- [43] G. A. Gehring and K. A. Gehring, Co-operative Jahn-Teller effects, *Rep. Prog. Phys.* **38**, 1 (1975).
- [44] M. D. Kaplan and B. G. Vekhter, *Cooperative Phenomena in Jahn-Teller Crystals*, Modern Inorganic Chemistry (Springer, Boston, 1995).
- [45] Q. Huang, J. L. Soubeyroux, O. Chmaissem, I. N. Sora, A. Santoro, R. J. Cava, J. J. Krajewski, and W. F. Peck, Neutron

- Powder Diffraction Study of the Crystal Structures of Sr_2RuO_4 and Sr_2IrO_4 at Room Temperature and at 10 K, *J. Solid State Chem.* **112**, 355 (1994).
- [46] T. Vogt and D. J. Buttrey, Temperature Dependent Structural Behavior of Sr_2RhO_4 , *J. Solid State Chem.* **123**, 186 (1996).
- [47] S. Klotz, J.-C. Chervin, P. Munsch, and G. Le Marchand, Hydrostatic limits of 11 pressure transmitting media, *J. Phys. D* **42**, 085413 (2009).
- [48] X. Xi, X. Bo, X. S. Xu, P. P. Kong, Z. Liu, X. G. Hong, C. Q. Jin, G. Cao, X. Wan, and G. L. Carr, Honeycomb lattice Na_2IrO_3 at high pressures: A robust spin-orbit Mott insulator, *Phys. Rev. B* **98**, 125117 (2018).
- [49] V. Hermann, J. Ebad-Allah, F. Freund, I. M. Pietsch, A. Jesche, A. A. Tsirlin, J. Deisenhofer, M. Hanfland, P. Gegenwart, and C. A. Kuntscher, High-pressure versus isoelectronic doping effect on the honeycomb iridate Na_2IrO_3 , *Phys. Rev. B* **96**, 195137 (2017).